Modelling contact angles with chemically specific dissipative particle dynamics

Guadalupe Jiménez-Serratos,*,† Patrick B. Warren,*,† Scott Singleton,‡ David J. Bray,† and Richard L. Anderson*,†

†*The Hartree Centre, STFC Daresbury Laboratory, Warrington, WA4 4AD, UK*

‡*Unilever R&D Colworth Laboratory, Sharnbrook, Bedford, MK44 1LQ, UK*

E-mail: lupe.jimenez-serratos@stfc.ac.uk; patrick.warren@stfc.ac.uk; richard.anderson@stfc.ac.uk

Abstract

We explore how walls can be introduced into chemically-specific dissipative particle dynamics (DPD) models such that the surface energies can be chosen to obtain a desired contact angle on a given substrate, for example for an oil/water interface. We certify the methodology for determining the surface energy, which can be positive or negative, such that the Young equation is automatically satisfied. We validate the approach against direct numerical simulation of cylindrical droplets of dodecane in water on the surface, and test it against an experimental model of a water droplet in dodecane on a surface-adsorbed monolayer on silica.

1 Introduction

Recent developments in dissipative particle dynamics (DPD) allow for the treatment of complex fluids and solutions of surfactants and polymers with chemical specificity, using a coarse-graining or fragmentation strategy in which the DPD 'beads' represent chemical

groups comprising typically 1–3 three 'heavy' atoms (carbon, oxygen, nitrogen, *etc*), with the exception of water which is treated supramolecularly (for details, see below). Although the 'force fields' (*i. e.* the non-bonded pairwise soft repulsions) are parametrised only against liquid phase density data and log P values,[1] these models have proven remarkably capable at capturing for instance the behaviour of surfactants, reproducing *inter alia* micelle formation and the critical micelle concentrations for nonionic and ionic surfactants,[2] the properties of surfactant mixtures,[3] and the phase behaviour of surfactants,[4] in a variety of industrially-relevant surfactant systems. With additional fine-tuning of the bonded interactions, the models are even capable of capturing the freezing transition ('waxing') of long-chain alkanes.[5,6] These developments build capabilities in the area of computer-aided formulation, and contribute an essential element to support the industry-wide move away from petrochemicals towards sustainably-sourced, ecologically and climate-friendly raw materials, and confronting what is a huge challenge for the multi-billion dollar surfactants business.

Most of the literature in this field is largely focused on the properties of bulk (liquid) materials, with less emphasis based on building substrate models, despite the latter's perhaps equal importance in numerous practical applications such as in laundry detergency, home and personal care products, emulsion and foam stability, and industrial separation processes. Indeed, even the basic question of how to parametrise substrates in chemically-specific DPD models has received scant attention to date. Whilst a few studies exist exploring the role of structure and patterns,[7] and heterogeneity,[8,9] studies which look to build chemically specific surface models (in DPD) do not yet appear in the literature. Here, we start to lay some foundations in this area by providing the basic building blocks for achieving some degree of specificity.

The focus of the present study is on the contact angle θ that the interface between two phases ('1' and '2') forms at the three-phase contact line on a solid substrate ('s') which is locally flat (Fig. 1).* Given the interfacial tension between the two phases of interest, γ_{12},

*The application of molecular simulations in estimating contact angles has recently been reviewed by Jiang and Patel [10]

and the surface energies of the two phases against the substrate, γ_{s1} and γ_{s2}, the contact angle satisfies the Young equation,[11,12]

$$\gamma_{s1} = \gamma_{s2} + \gamma_{12}\cos\theta\,. \tag{1}$$

There are various ways to derive this result (for example, see Appendix), but at its simplest one can view it as a static force balance as indicated in Fig. 1b.

For the contact angle to be finite (*i. e.* $0 < \theta < 180°$), one must have $|\gamma_{s1} - \gamma_{s2}| < \gamma_{12}$. An alternative way to view this is to consider the de Gennes spreading parameter,[12,13]

$$S \equiv \gamma_{s1} - \gamma_{s2} - \gamma_{12}\,. \tag{2}$$

With this definition, the Young equation can be written

$$S = \gamma_{12}(\cos\theta - 1)\,. \tag{3}$$

If we consider phase '2' to be a droplet, as shown in Fig. 1a, this makes it clear that there are three domains of behaviour,

$S > 0$	$\cos\theta = 1$	complete wetting	droplet spreads out,
$-2\gamma_{12} \le S \le 0$	$\lvert\cos\theta\rvert \le 1$	partial wetting	finite contact angle,
$S < -2\gamma_{12}$	$\cos\theta = -1$	complete dewetting	droplet detaches.

The spreading parameter S is therefore a measure of the wettability of the substrate by the indicated phases.

Under conditions of partial wetting the contact angle θ is directly accessible to experiment. As such, it is directly relatable to many of the above-mentioned practical applications: for example laundry detergents are designed to promote a high contact angle or even complete detachment for an oil droplet on a surface, facilitating disproportionation and roll-up;[14]

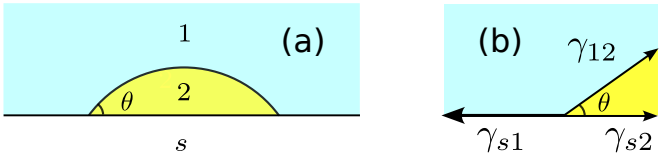

Figure 1: Example of a contact angle (a), and the geometry of the Young equation (b).

antifoams depend on the partial wettability of hydrophobic particles to cause film breakage;[15] in a Pickering emulsion, particles with a judiciously chosen contact angle sit on the interface and stabilise oil droplets;[16] and in mineral flotation, differential wettability is used to separate the valuable ore from the unwanted 'gangue' components.[17]

For coarse-grained particle-based simulation methodologies such as our chemically-specific DPD models, there are two approaches to modelling walls. The first is simply to extend the particle-based paradigm to represent a wall as an array of DPD beads which are either 'frozen', or tethered to fixed sites.[7,9] In this, one can take advantage of the bead-bead interactions already derived within a standard parametrisation strategy, but on the other hand the determination of the surface energies may be delicate. Additionally, there is the need to choose the density and arrangement of the beads, and parametrise the tethering force if the beads are not frozen. Such an approach could however be suitable for materials which are chemically patterned or have nanoscale roughness. An alternative approach, which is the focus here, is to model the surface as a smooth, featureless substrate. This approach is suitable for atomistically or molecularly smooth materials, such as glass (silica), many plastics (for example, polythene, polypropylene, polyester), minerals (calcite, hydroxyapatite, *etc*), organic crystals such as sugars (sucrose), and perhaps even ice. Within this approach, which pertains to many situations of direct practical relevance, the parametrisation problem becomes simply one of designating the wall forces for each bead type in the bulk. Moreover, determination of the surface energies is very straightforward as we shall see.

Whichever wall model is adopted, our central thesis is that it should recover the macro-

scopic contact angle(s) for droplets of given liquids on the substrates of interest, and at the same time it should minimally perturb the liquid structure on length scales beyond the immediate vicinity of the wall. The reasoning behind the first requirement is that in the absence of directly measured surface energies, contact angles stand in for the wettability of the substrate. For example, in saying that a surface is hydrophilic or hydrophobic one is really making a statement about the contact angle of a droplet of water on that surface (whilst the present work does not cover vapor-liquid interfaces, the methods we develop should be equally applicable). For the second requirement, we note that if a coarse-grained DPD water bead represents several actual water molecules, structure on the bead length scale induced by the wall (*e. g.* oscillations in the bead density) should be minimised. This latter requirement involves an inevitable trade off in being able to set surface energies arbitrarily, but as a design criterion it can be used to narrow the choice of wall interaction potentials as described below, and take advantage of a built-in degree of freedom since in determining contact angles it is only the *difference* in surface energies, $\gamma_{s1} - \gamma_{s2}$, that is relevant for the Young equation and the de Gennes spreading parameter.[12]

In this article we outline the chemically-specific DPD model that we use as a basis, and describe the wall model that we use. We then introduce the methodology for calculating the surface energies from our DPD simulations such that the Young equation is automatically satisfied. Next, we validate this against direct numerical simulations of oil droplets on surfaces, using dodecane in water at 25 ℃ as our model. Finally, we consider the complementary case of a water droplet in oil, and show that our methodology can reproduce the case of a water droplet in dodecane on a surface-adsorbed monolayer on silica.

2 Chemically-specific DPD

2.1 Model Building

We adopt the DPD parameters from Anderson *et al.*[1] Here, each DPD bead represents a chemical group comprising $n = 1$–3 'heavy atoms' (*e. g.* carbon, oxygen), except for water, which is treated super-molecularly, with the DPD water bead representing two water molecules ($2\,H_2O$). Dodecane ($C_{12}H_{26}$) is represented as a 7-mer, $CH_3{-}(CH_2CH_2)_5{-}CH_3$, consisting of CH_2CH_2 and terminal CH_3 beads. Note that under atmospheric pressure dodecane has a melting point of about $-10\,℃$, so it is liquid under the conditions of the simulations.

The non-bonded interactions (*i. e.* the DPD conservative force) are defined by standard DPD pairwise soft repulsions of the form,[18,19]

$$U_{ij}(r_{ij}) = \begin{cases} \frac{1}{2}A_{ij}(1 - r_{ij}/R_{ij})^2 & (0 < r_{ij} < R_{ij})\,, \\ 0 & (r_{ij} \geq R_{ij})\,, \end{cases} \tag{4}$$

where A_{ij} and R_{ij} are the repulsion amplitude and range, and $r_{ij} = |\vec{r}_j - \vec{r}_i|$ is the separation between beads i and j located at $\vec{r}_i$ and $\vec{r}_j$ respectively. The repulsion amplitude for water beads is set to $A_{ij} = 25$, and likewise by convention $R_{ij} = 1$ for water beads, in units of r_c, the fundamental unit of length in our model.

We establish the latter by mapping our bead model of pure water at a bead density $\rho r_c^3 = 3$ to real water using Avogadro's constant N_A, the molar mass of a water bead $M(2\,H_2O) \approx 36\,g\,mol^{-1}$ (noting there are two water molecules per bead), and the mass density of water $\varrho_w \approx 1000\,g\,L^{-1}$. From this we infer that

$$N_A r_c^3 = \frac{\rho r_c^3\, M(2\,H_2O)}{\varrho_w} \approx 0.108\,L\,mol^{-1}\,, \tag{5}$$

and hence $r_c \approx 0.564\,nm$. Note that with Eq. (5) we can convert a bead density in DPD

Table 1: DPD repulsion amplitudes and cut-off distances for the three bead types used in this work obtained from Anderson *et al.*[1]

bead i	bead j	A_{ij}	R_{ij}
$2\,H_2O$	$2\,H_2O$	25.0	1.0000
$2\,H_2O$	CH_2CH_2	45.0	1.0370
$2\,H_2O$	CH_3	45.0	0.9775
CH_2CH_2	CH_2CH_2	22.0	1.0740
CH_2CH_2	CH_3	23.0	1.0145
CH_3	CH_3	24.0	0.9550

units to a real density by multiplying by $M(\text{bead})/N_A r_c^3$, where $M(\text{bead})$ is the molar mass.

The remaining bead parameters are given in Table 1, and are tuned to reproduce the experimental liquid phase densities and water-octanol partition coefficients ($\log P$ values) for a range of small molecules. The cut-off distance for the dissipative and random forces required in the DPD method was assigned equal to the maximum cut-off distance in the system (*i. e.* supremum $(\{R_{ij}\}) = 1.0740$) and the dissipative friction amplitude was set at 4.5.

For the bonded interactions, a simple harmonic potential $U_{ij}^B = \frac{1}{2}k_b(r - r_0)^2$ is used between connected DPD beads, with r_0 equal to 0.29 and 0.39 for $CH_3{-}CH_2CH_2$ and $CH_2CH_2{-}CH_2CH_2$ respectively, and a single bond constant $k_b = 150$ (DPD units) adopted throughout. To stiffen the molecules we introduce bond rigidity by including a harmonic angular potential between pairs of bonds. We adopt the three-body angular potential used by Smit and collaborators,[20,21] namely $U_{ijk}^A = \frac{1}{2}k_a(\theta - \theta_0)^2$ where θ is the angle between adjoining bonds and we adopt $\theta_0 = 180^\circ$ and $k_a = 5$ (DPD units) for all angles.

2.2 Wall model

We now turn to the specification of the wall model. As mentioned in the introduction, in our approach we treat this as a smooth, featureless substrate which interacts with the DPD

beads through bead-specific wall potentials. For instance, consider a wall located at the $z = 0$ plane. We suppose generally there is a hard reflecting barrier at $z = 0$, so that DPD particles cannot penetrate to $z < 0$. This is implemented in the simulation using specular (mirror-like) reflection (rather than bounce-back reflections). For $z > 0$ we augment this with a soft, short-range potential of the form,[22]

$$U_{s,i}(z_i) = \begin{cases} \frac{1}{2}A_{s,i}(1 - z_i)^2 & (0 < z_i < 1)\,, \\ 0 & (z_i \geq 1)\,, \end{cases} \tag{6}$$

where z_i is the height of the i-th particle above the hard reflecting boundary at $z = 0$. We set the wall potential to have the same functional form for all bead types, but differentiate these from each other by bead-specific repulsion amplitudes $A_{s,i}$, intended to capture the surface chemistry. For simplicity we set the range here equal to unity (in units of r_c) for all bead types though one could envisage this being used as an additional fine-tuning parameter. We anticipate that the exact functional form of the wall potential is unimportant as long as it remains soft and short-ranged, so we have chosen something for numerical convenience which is similar to the pair interactions in Eq. (4).

Again for simplicity, in the present study we do not distinguish between the two alkane bead types, so we only consider wall repulsion amplitudes $A_{s,\mathrm{dod}}$ where 'dod' (for dodecane) represents both CH_3 and CH_2CH_2 beads, and $A_{s,\mathrm{wat}}$ where 'wat' refers to the water beads. These repulsion amplitudes were varied from zero to 50 in steps of 10 (in a matrix) to observe the effect of the interaction strength upon the structure and surface energies for each of the two liquids, water and dodecane.

2.3 Simulation conditions

2.3.1 General simulation conditions

All simulations were run using the DL_MESO simulation package (version 2.8),[23] at a reduced temperature of T = 1.0 (which is equivalent to 25 °C according to the underlying parameterization). A time step of 0.02 (DPD units) was used through out. For NPT simulations a Langevin-piston barostat was used, with $p = 23.7$ in reduced units to correspond to the pressure in our bead model of pure water at a reduced density $\rho r_c^3 = 3$.

We note that since $k_\mathrm{B}T/r_c^3 = RT/N_A r_c^3 \approx 2.3 \times 10^7\,\mathrm{Pa}$ at $T = 298\,\mathrm{K}$, in real units the operating pressure $23.7\,k_\mathrm{B}T/r_c^3 \approx 0.54\,\mathrm{GPa}$. This is much larger than atmospheric pressure (100 kPa). We accept this, noting that unlike typical real liquids, there is no cohesive contribution to the interparticle forces in DPD to reduce the 'overpressure'.

We have found that at $P = 23.7$ the reduced density of pure DPD dodecane is $\rho r_c^3 \approx 3.27$. Since in this DPD model dodecane is a 7-mer, the mean molar mass of a dodecane bead is $M(\mathrm{C_{12}H_{26}})/7 \approx 24.3\,\mathrm{g\,mol^{-1}}$. Utilising Eq. (5), this corresponds to a real mass density $3.27 \times 24.3/0.108 \approx 740\,\mathrm{g\,L^{-1}}$, which is within 1.5% of the true value of $750\,\mathrm{g\,L^{-1}}$. This is expected since the DPD parameters are tuned to reproduce liquid phase densities.

2.3.2 Liquid-liquid interface

Each system utilised an initial simulation cell of size $L_x \times L_y \times L_z = 10 \times 10 \times 200$. This size was settled upon after performing calculations for a series of different box sizes to ensure finite size effects are ruled out. Further information regarding these effects can be found in the Supporting Information. For the dodecane–water system, the initial simulation setup was constructed such that each of the two components were placed in either half of the simulation cell. Periodic boundary conditions were adopted in all three dimensions. In this case, the oil–water system comprises two interfaces, one at $z \approx L_z/2$ and one at $z \approx 0$. In the final result, whilst equal in number of beads, water and dodecane occupy slightly different

volumes due to their different densities. All simulations to determine the interfacial tension values were performed initially under a NPT ensemble at starting reduced density of $\rho = 3.0$. Subsequently, NVT simulations were completed (at the equilibrium simulation box lengths from NPT calculations) to ensure agreement in results. Both ensembles produced results in agreement within the reported error of each other.

For comparison and to provide a benchmark, additional molecular dynamics (MD) simulations were performed at a temperature of 300 K using the TIP4P/2005 water model,[24] and dodecane obtained using the optimised L-OPLS parameters of Siu *et al.*[25] A system containing 1600 dodecane and 20 500 water molecules (corresponding to a final box size of $L_x = L_y = 8.5$ nm and $L_z = 17.1$ nm) was initially run for 5 ns (using a time step equal to 0.001 ps) under the anisotropic NP_zT ensemble, in which the L_x and L_y dimensions are fixed and L_z fluctuates to reach the pressure of 1 bar, using the Parrinello-Rahman barostat and Nosé-Hoover thermostat. The system was further run at NVT conditions for 20 ns and the final 10 ns were used for data collection.

2.3.3 Liquid-surface interface

For the liquid–surface systems molecules comprising the liquid were placed randomly in a simulation cell equivalent in size to the dodecane–water system, defined above. The same simulation protocol as above was used except that the semi-periodic boundary conditions were employed in the xy dimensions and substrate walls are placed at $z = 0$ and $z = L_z$. The properties of the upper wall are identical to the lower wall, with suitable reflection and translation.

2.3.4 Droplet on surface

To study the explicit droplets, we performed NVT simulations containing the same surface as described above, parallel to the xy plane. The initial configuration consisted of dodecane molecules within a rectangular parallelepiped region at the reduced dodecane bead density

of $\rho = 3.27$ in DPD units, located on the surface at $z = 0$, centred in x and extending along the y axis. The rest of the simulation box is filled by DPD water beads at a reduced density $\rho = 3$. The visualisation of an initial configuration is presented in Fig. 2a. The distance between the walls L_z is large enough to avoid interactions between dodecane molecules and the upper surface. We select interaction parameters $A_{s,\alpha}$ to produce a variety of contact angles in the explicit systems. The simulations are equilibrated for 5×10^5 time steps to allow the dodecane region adopt a cylindrical shape (see Fig. 2a, right-hand panel). Once equilibrium is reached, production simulations of 10^6 time steps are performed and every 10^3 time steps the configuration is saved to a trajectory file for analysis.

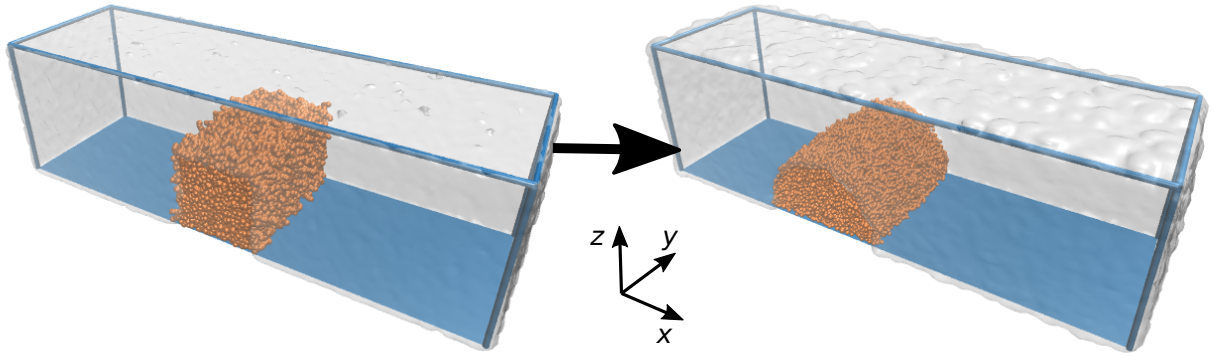

(a) Explicit droplet simulation setting

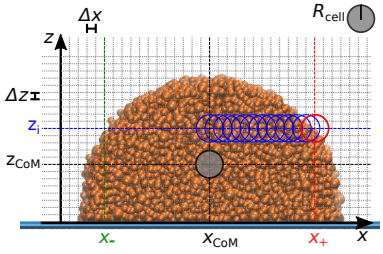

(b) Identifying droplet boundary

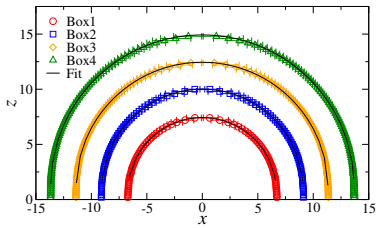

(c) circle arc fitting

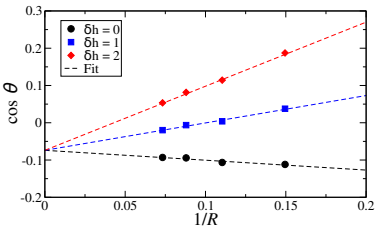

(d) extrapolation to $R \to \infty$

Figure 2: Stages required to measure $\cos\theta_{\text{sim}}$ in explicit droplet simulations. Here we show (a) the initial and final simulation configuration, were water beads are represented as a transparent surface for clarity, (b) a schematic representation of the algorithm to obtain the discrete droplet profile in the xz plane, (c) the circle-arc profile from systems of different box sizes using $A_{s,\text{dod}} = A_{s,\text{wat}} = 50$, and (d) a demonstration of the interface position δh effect on the extrapolation to infinite droplet radius using the same data in (c).

For every surface model, we study four simulation boxes to produce droplets of different

Table 2: Details of simulation boxes for the explicit droplet simulations of dodecane droplets water. The box size (L_x, L_y, L_z), and size of the dodecane regions (l_x, l_y, l_z), are given in DPD units. The final columns report the number of dodecane molecules (DPD 7-mers), the number of DPD water beads, and the total number of DPD beads.

Box ID	$(L_x,\ L_y,\ L_z)$	$(l_x,\ l_y,\ l_z)$	N_{dod}	N_{wat}	N_{tot}
Box1	(50, 20, 25)	(8, 25, 8)	907	69 164	75 513
Box2	(50, 20, 25)	(11, 25, 11)	1679	64 197	75 950
Box3	(100, 30, 30)	(14, 30, 14)	3115	249 958	271 763
Box4	(100, 30, 30)	(17, 30, 17)	4512	240 970	272 554

diameters. In Table 2, we give size and composition details: total dimensions (L_x, L_y, L_z), the size of the initial dodecane region (l_x, l_y, l_z), the number of dodecane molecules N_{dod} (DPD 7-mers), the number of DPD water beads $N_{\mathrm{wat}} = N_{\mathrm{H_2O}}/2$, and the total number of DPD beads in every box $N_{\mathrm{tot}} = 7N_{\mathrm{dod}} + N_{\mathrm{wat}}$.

From the balance between viscous dissipation and surface tension, the time for the droplet to reach its final shape can be estimated as $\eta R/\gamma$ where η is the fluid viscosity, γ is the interfacial tension, and R is the droplet diameter.[13] Since we expect η and γ to be $O(1)$ in DPD units, and R is at most several tens of r_c (Table 2), this time scale is perhaps 10–100 DPD time units, or not more than 10^3–10^4 DPD time steps. Hence the equilibration time of 5×10^5 time steps should be ample to allow the droplet to reach its final cylindrical shape. This is in accord with our observations.

2.4 Measurement

2.4.1 Liquid-liquid interfacial tension determination

The approach to calculating the liquid-liquid interfacial tension is well established,[26] and uses the volume- and time-averaged diagonal components of the pressure tensor, $\langle P_{xx}\rangle$, $\langle P_{yy}\rangle$, and $\langle P_{zz}\rangle$, as

$$\gamma_{12} = \frac{L_z}{2}\Big(\langle P_{zz}\rangle - \frac{1}{2}(\langle P_{xx}\rangle + \langle P_{yy}\rangle)\Big)\,. \tag{7}$$

Here L_z is the length of the simulation box in the direction perpendicular to the liquid-liquid interface, assumed to be the z-direction and the outer factor '2' derives from the fact that in periodic boundary conditions there are two interfaces. In a bulk region all three components of the pressure tensor become equal to each other and equal to the bulk pressure, $P_{xx} = P_{yy} = P_{zz} = p$. A non-zero value for γ_{12} (which must be positive) results from the fact that $P_{xx} = P_{yy}$ (assuming in-plane isotropy) deviates negatively from $P_{zz} = p$ in the interfacial region, where the constancy of the latter derives from mechanical equilibrium. Typically, the negative deviation in the lateral components of the pressure tensor corresponds to a 'dip' in the density profiles in the interface, with fewer particles, reduced lateral forces and reduced lateral momentum transport in this region.

2.4.2 Liquid-substrate surface energy determination

In contrast, determination of the surface energy for a fluid against a wall can be fraught with difficulties due to the presence of internal stresses in the solid substrate. To overcome these, Leroy and coworkers devised a 'phantom wall' method to compute the surface energy.[27–29] By incrementally 'lifting' the phantom wall off the real substrate, one can compute the difference in surface energy between the real wall and the phantom wall by thermodynamic integration. This is augmented by a direct calculation of the phantom wall surface energy once the real wall is sufficiently distant to avoid perturbing the fluid.

In our model the introduction of a phantom wall and the thermodynamic integration step are unnecessary since the wall is structureless, there are no internal stresses, and the wall forces are always normal to the surface. As a result, we can show that Eq. (7) can also be used for the wall surface energies, provided an augmented definition $\langle P'_{zz} \rangle$ is used which includes the wall forces. The details are given in the Appendix.

Importantly, the surface energy thus computed can be positive *or negative*. The reason is that there does not have to be a diminishment in $P_{xx} = P_{zz}$ at the wall. In fact, the particle density profile can show an excess, for example for a pure hard wall without any additional

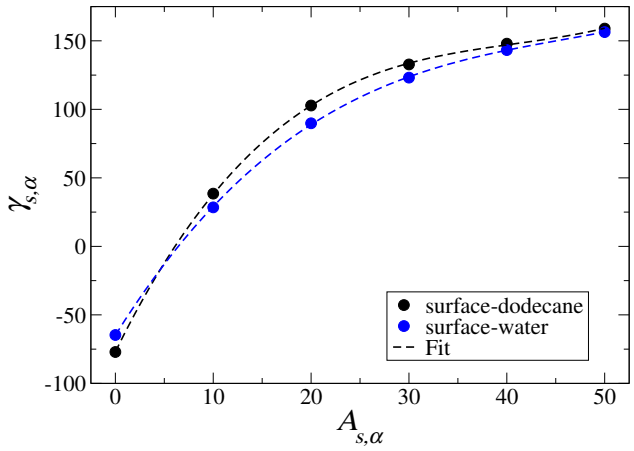

Figure 3: Surface energies in $\mathrm{mN\,m^{-1}}$ for dodecane and water using different surface-fluid interactions (circles), together with fits to third-degree polynomials (dashed lines).

repulsive force. In such a situation particles pile up in the vicinity of the wall because a part of the *transverse* repulsions between particles are missing, as a consequence of particles being excluded from the $z < 0$ and $z > L_z$ regions.

During the simulation we measure the pressure tensor every 50 timesteps, obtained as output of DL_MESO, and incorporating the contribution of the wall forces as described in the Appendix. This is the default position in DL_MESO 2.8 onwards but not for earlier versions of the package.

2.4.3 Droplet contact angle

To obtain the contact angles from an explicit droplet, we perform the following steps. First, we identify the droplet boundary following the schematic representation in Fig. 2b. We start by locating the droplet centre of mass (CoM) onto the xy plane. The local density of a cylindrical cell centred at the CoM is stored as a reference value $\rho_{\mathrm{ref}} = \rho(x_{\mathrm{CoM}}, z_{\mathrm{CoM}})$, using a cell radius of $R_{\mathrm{cell}} = 1.5$. The local dodecane densities are calculated by moving the centre of the sampling cell on a grid with $\Delta x = \Delta z = 0.2$, starting from the base of the droplet (by the surface) to the droplet's apex. The discrete profile boundary at height z_i is determined as the position of the first cell to the left ($x_-(z_i)$) and right ($x_+(z_i)$) from x_{CoM} which satisfies

Table 3: Substrate surface energies, in $\mathrm{mN\,m^{-1}}$, for various wall interaction strengths. α represents any bead species in water and dodecane. Results correspond to valuse obtained for a cell of size $L_x \times L_y \times L_z = 10 \times 10 \times 200$. The figure in brackets is an estimate of the error in the final digit.

$A_{s,\alpha}$	$\gamma_{s,\mathrm{dod}}$	$\gamma_{s,\mathrm{wat}}$
0	−77.1(5)	−64.7(4)
10	38.5(5)	28.5(4)
20	102.8(5)	89.8(4)
30	132.8(5)	123.1(4)
40	147.9(5)	143.3(4)
50	158.9(5)	156.4(4)

$\rho(x_k, z_i)/\rho_{\mathrm{ref}} < 0.5$.

With the droplet boundaries defined, a circular arc can be fitted around the perimeter. The profile points close to the top of the drop present larger error bars due to the density fluctuations in that region (Fig. 2), hence, we discard some of those profile points with the criterion of using only data with less than 10 % of relative error. For the remaining data, we use the algorithm presented in Thomas and Chan[30] based on the Landau method to obtain the radius R and centre (x_c, z_c) of the circle arc.

The contact angle $\theta_{\mathrm{sim}}(R)$ is obtained from

$$x_c + \delta h = R \cos\theta_{\mathrm{sim}}(R) \tag{8}$$

where δh is the interface position. Finally, for every set of parameters, we exploit the linear dependence of R in Eq. (8) to extrapolate out to $R \to \infty$ and obtain $\theta_{\mathrm{sim}} \equiv \theta_{\mathrm{sim}}(R \to \infty)$. We present a test of the sensitivity to δh in Fig. 2d using the systems with $A_{s,\mathrm{wat}} \equiv A_{s,\mathrm{dod}} = 50$. We observe that, while the individual $\cos(\theta_{\mathrm{sim}})$ values are affected by the δh selection, the dependence is lost in the macroscopic droplet extrapolation, $R \to \infty$. This is compatible with the observations in Zhang *et al.*[31], where comprehensive discussion on the topic is presented. The final analysis of all simulation sets is performed using $\delta h = 2$ in DPD units.

3 Results and Discussion

3.1 Interfacial tension and surface energies

In this section we use DPD simulations to determine the interfacial tension and surface energies that are required in the Young equation, Eq. (1), using the volume-average pressure tensor components in Eq. (7) as detailed above. We convert the results from DPD units to real units by multiplying by the factor $k_{\mathrm{B}}T/r_c^2 = r_c \times RT/N_A r_c^3 \approx 12.9\,\mathrm{mN\,m^{-1}}$, on the basis of Eq. (5) and assuming $T = 298\,\mathrm{K}$.

From simulations of the dodecane/water system (without walls) we calculate the dodecane/water interfacial tension to be $\gamma_{\mathrm{wat,dod}} = 27.3 \pm 0.4\,\mathrm{mN\,m^{-1}}$. Despite the large background 'overpressure' (Sec. 2.3.1), this is comparable to, but somewhat lower than the experimentally reported 51–52 $\mathrm{mN\,m^{-1}}$ range that is typical for this system.[32,33] We attribute the mismatch between our simulated results and experimental data to a rather thick liquid-liquid interfacial region (solid lines in Fig. 4a), which is a consequence of the soft potentials typically employed in DPD.

A number of DPD studies report models where the interfacial tension for oil–water systems closer to experimental data. In these works, both oil and water are often represented as single beads and the repulsion amplitude describing the interaction between the two solvents is then set to a large value, *e. g.* $A_{\mathrm{wat,oil}} \approx 100$ in order to reproduce the experimental interfacial tension.[34–36] Using a larger value for A_{ij} has the effect of sharpening up the transition in the liquid density at the interface. We can reproduce this effect in our model by increasing the repulsion amplitude between water and dodecane beads (both types) from $A_{\mathrm{wat,dod}} = 45$ (solid lines in Fig. 4a) to 100 (dashed lines in Fig. 4a). With this increased repulsion amplitude we find $\gamma_{\mathrm{wat,dod}} = 54.5 \pm 0.3\,\mathrm{mN\,m^{-1}}$, which is adjusted to be close to experiment. Such large changes in the oil-water interaction parameters would render our model useless in its ability to reproduce partition coefficients and liquid phase densities for

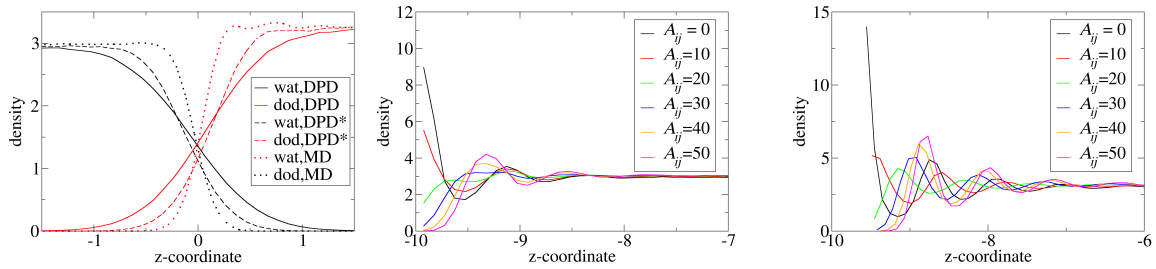

(a) water–dodecane (b) water–surface (c) dodecane–surface

Figure 4: Liquid bead number concentration profiles perpendicular to the interface, water phase giving way to dodecane phase in (a) and with surface placed at lower z boundary in the case of (b,c). For (a) we show the water-dodecane interface for three scenarios; (i) resulting from the original DPD parameters (solid lines); (ii) resulting from an increase in the water-dodecane repulsion parameter (from 45 to 100, denoted by an $*$ in the legend); (iii) resulting from MD simulations. For details of the simulations carried out, please refer to the main text. For (b) and (c) we show the concentration profile for each liquid with the surface at varying A_{ij} values.

which the model was originally parameterised though. To explore this still a little further, we compare these results from the two DPD models with an MD simulation of a dodecane-water interface (dotted lines in Fig. 4a). The resultant MD value of the water-dodecane interfacial tension was $\gamma_{\mathrm{wat,dod}} = 56 \pm 3\,\mathrm{mN\,m^{-1}}$. We observe (Fig. 4a) that in the MD simulation the interface width is even narrower than the artificially sharpened DPD model.

Now we turn to the substrate surface energies, using simulations of either pure water or pure dodecane, confined between parallel walls as described in Sec. 2.4.1. Table 3 and Fig. 3 show how the surface energies for water and dodecane varies with the surface repulsion amplitude $A_{s,\alpha}$ (where α is either dodecane or water). For both liquids, the value of $\gamma_{s,\alpha}$ increases strongly as expected. In the case where the interaction between the surface and the liquids are set to zero, the recorded surface energies are large and negative ($\gamma_{s,\mathrm{wat}} = -64.7\,\mathrm{mN\,m^{-1}}$ and $\gamma_{s,\mathrm{dod}} = -77.1\,\mathrm{mN\,m^{-1}}$). Figs. 4b and 4c present the density profiles of the water and dodecane liquids at the surface with increasing $A_{s,\alpha}$. For both liquids significant ordering results with dodecane being more strongly affected than water. Ordering in the case of water persists for ≈ 2 DPD distance units and for dodecane this is increased to ≈ 3 units. Surface induced ordering is minimized for both liquids at $A_{s,\alpha} \approx 20$.

Table 4: Comparison of contact angles obtained via the Young equation and explicit droplet simulations. The figure in brackets is an estimate of the error in the final digit.

$A_{s,\mathrm{wat}}$	$A_{s,\mathrm{dod}}$	θ [°] (Young)	θ [°] (droplet)
10	10	111(4)	108(3)
30	30	111(3)	105(3)
30	40	155(2)	141(5)
40	30	67(3)	64(2)
40	40	100(2)	99(3)
40	50	125(3)	122(4)
50	40	72(2)	72(2)
50	50	95(2)	94(3)

3.2 Validation of contact angle prediction

We now validate our approach by comparing the contact angles predicted by the Young equation with measurements of the contact angles from our explicit droplet simulations. For the latter, examples of the $\cos\theta_{\mathrm{sim}}(R)$ values and linear extrapolations are presented in Fig. 5 for selected cases. We include snapshots of the largest droplet in equilibrium for every case and omit the error bars, which are smaller than the symbols.

Table 4 shows the comparison between the contact angles predicted from the Young equation using the water/dodecane interfacial tension $\gamma_{\mathrm{wat,dod}} = 27.3 \pm 0.4\,\mathrm{mN\,m^{-1}}$ (*i. e.* using our original parameter set in Table 1) plus the surface energies reported in Table 3, and the contact angles extrapolated from explicit droplet simulations by the described method, for a variety of $A_{s,\alpha}$ combinations. A good agreement is found with a relative error under 4 %. In Fig. 6, we show a scatter plot of the data.

To extend the tests to other surface-fluid interactions, we fit the discrete values of $\gamma_{s,\alpha}$ (in real units of $\mathrm{mN\,m^{-1}}$) as a function of $A_{s,\alpha}$ to third-order polynomials,

$$\gamma_{s,\mathrm{dod}} = -76.9 + 14.6\,A_{s,\mathrm{dod}} - 0.333\,A_{s,\mathrm{dod}}^2 + 0.00272\,A_{s,\mathrm{dod}}^3\,, \tag{9a}$$

$$\gamma_{s,\mathrm{wat}} = -64.8 + 11.4\,A_{s,\mathrm{wat}} - 0.218\,A_{s,\mathrm{wat}}^2 + 0.00156\,A_{s,\mathrm{wat}}^3\,. \tag{9b}$$

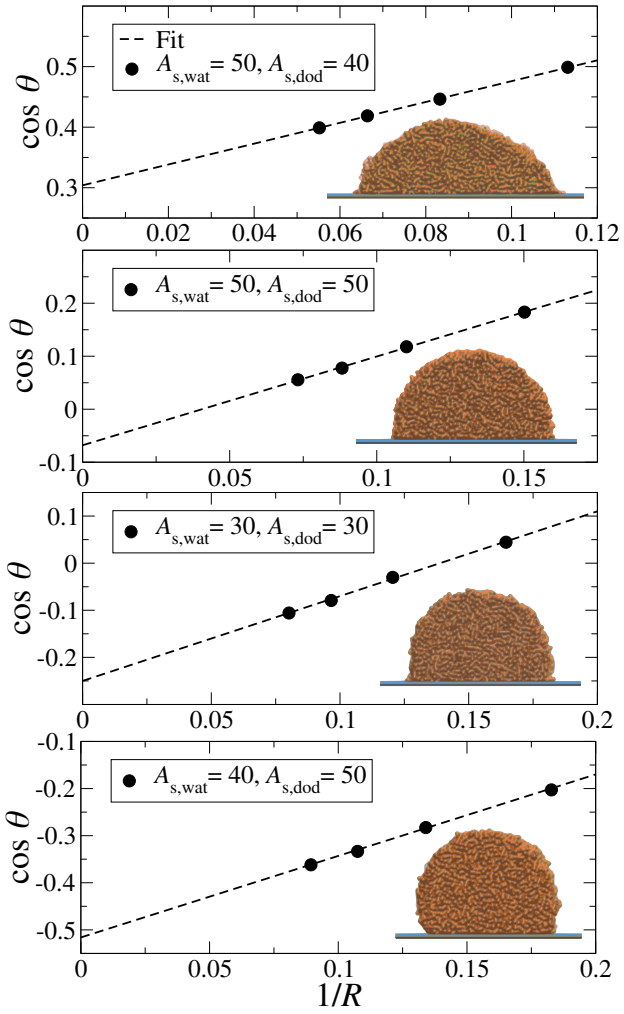

Figure 5: $\cos\theta_{\mathrm{sim}}(R)$ values obtained from explicit droplet simulations of different sizes. The dashed lines represent the linear extrapolation to the macroscopic radius, $R^{-1} \to 0$. Inserted in the plot, a visualisation of the largest system is shown for every pair of wall-fluid interactions.

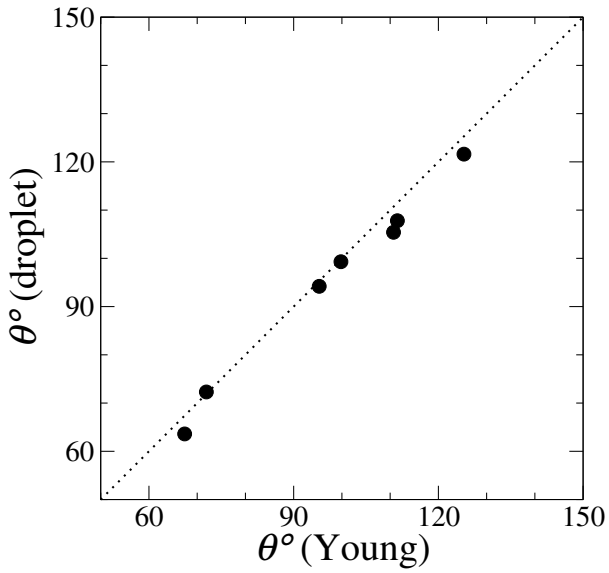

Figure 6: Contact angles measured in droplet simulations (vertical axis) plotted against the values predicted by the Young equation (horizontal axis).

The coefficient of determination was $R^2 = 0.9999$ in both cases, since the dependence is rather smooth and these fits are quite accurate as shown in Fig. 3. The coefficients in these expressions differ because dodecane in our DPD model is a molecular fluid at a different density, and with different bead interactions, than the DPD water model.

These fits allow us to represent the contact angles from the Young equation as a surface, see Fig. 7b. Using the discrete $\gamma_{s,\mathrm{wat}}$ values, 2D projections of the contact angle as a continuous function of $A_{s,\mathrm{dod}}$ are shown in Fig. 7b, dashed lines. We employ this plot as a guide to select $(A_{s,\mathrm{wat}}, A_{s,\mathrm{dod}})$ combinations and simulate explicit droplet systems. The resulting contact angles correspond to the solid symbols in Fig. 7b. We observe a good agreement finding an average relative error of 5 % when comparing both approaches.

Combinations of $(A_{s,\mathrm{wat}}, A_{s,\mathrm{dod}})$ that produced contact angles under 30° were challenging to simulate since the explicit droplets tend to spread out, in particular, for the smaller system sizes. Other combinations generated detached droplets that we did not analyse. To understand these behaviours, we return to the de Gennes spreading parameter defined in Eq. (2). Here, we use the smoothed versions of surface energies in Eqs. (9) to calculate S

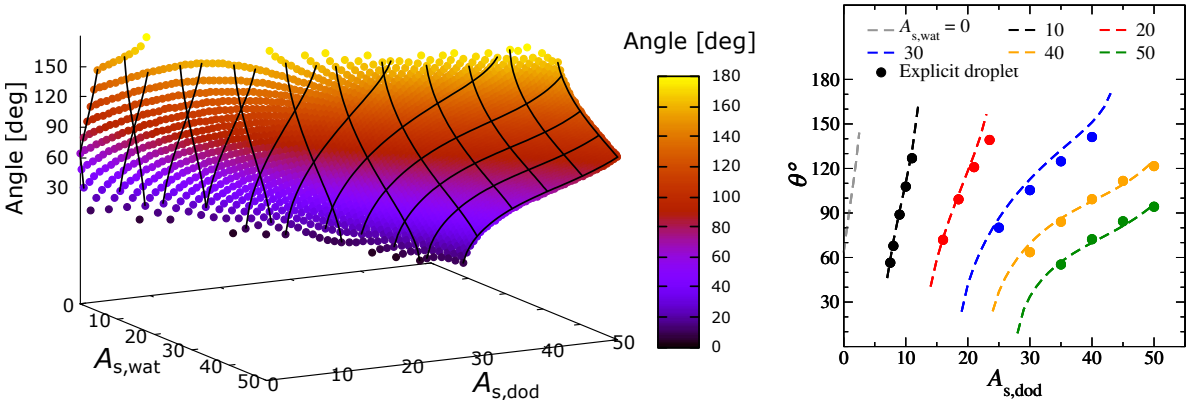

(a) Contact-angle surface (b) Comparison of methods

Figure 7: Contact angles obtained from the Young equation. (a) Surface representation using smooth values of $\gamma_{s,\mathrm{wat}}$ and $\gamma_{s,\mathrm{dod}}$, and (b) 2D representation using the smooth $\gamma_{s,\mathrm{dod}}$ in the Young equation (dashed lines) and comparing it to explicit droplet simulations (filled circles).

as a function of $(A_{s,\mathrm{wat}}, A_{s,\mathrm{dod}})$, noting that for this purpose $\gamma_{\mathrm{wat,dod}} = 27.3 \pm 0.4\,\mathrm{mN\,m^{-1}}$ is a constant dictated by the coarse-grained water-plus-dodecane model. Fig. 8 shows the behaviour of the droplet on the surface as predicted by S. Corresponding to the classification scheme in the introduction, three regimes are observed. In the lower right region, $S > 0$ and the droplet spreads out. In the upper left region, $S < -2\gamma_{\mathrm{wat,dod}}$ corresponds to droplet detachment. In the middle region, where $-2\gamma_{\mathrm{wat,dod}} < S < 0$, partial wetting is observed, with the droplet sitting on the surface with a finite contact angle as indicated by the color scale. The boundary between the droplet spreading regime and finite contact angle regime corresponds to the boundary we have seen in the simulations.

These behaviours follow common sense, since increasing $A_{s,\alpha}$ increases the surface energy of the corresponding phase. Thus, generally, the surface tends to favour the phase with the smaller value of $A_{s,\alpha}$. Finally, we note that the map in Fig. 8 is asymmetric for the same reason that the polynomial fit coefficients in Eqs. (9) are different: in our model water and dodecane are different liquids with different densities and different bead interactions.

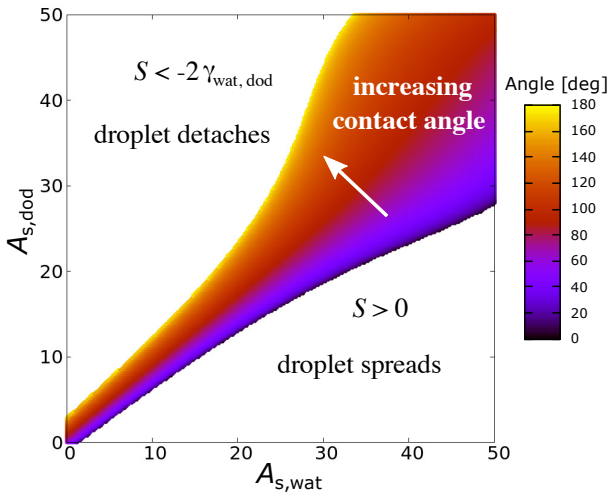

Figure 8: Map of droplet behaviours on the surface as a function $(A_{s,\mathrm{wat}}, A_{s,\mathrm{dod}})$, as determined by the de Gennes spreading parameter S.

3.3 Application: tuning the hydrophobicity of model surfaces

In this section, we employ the Young equation to parametrise surfaces with different degrees of hydrophobicity. As a benchmark, we use experimental contact angles of water droplets in dodecane in silica surfaces obtained by Andersson *et al.*[37] In these experiments, silica wafers are modified with self-assembled monolayers (SAMs) of different compositions, affecting the wettability. Here, we take three combinations of –OH and $-CH_3$ coverages (see first and second columns in Table 6) and propose a simple continuous wall model for each.

We begin with Eq. (1), where the droplet is now made of water and the surrounding liquid dodecane. The two phase simulations required to obtain the interfacial tension for the Young equation are the same cases presented in Sec. 3.1. In analogy to the previous section, we use the discrete $\gamma_{\mathrm{s,dod}}$ values and the smooth version of $\gamma_{\mathrm{s,wat}}$, Eq. (9b), to plot the contact angles from the Young equation as a continuous function of $A_{\mathrm{s,wat}}$, Fig. 9a. To generate continuous wall models with effective interactions, we follow the steps represented in the same figure: A) select and fix $A_{\mathrm{s,dod}} = 30$, leaving $A_{s,\mathrm{wat}}$ to reflect the hydrophilic or hydrophobic effect introduced by the surface modifications; B) locate the experimental contact angles in the curve and C) find the corresponding $A_{s,\mathrm{wat}}$ value. The effective surface-water interactions

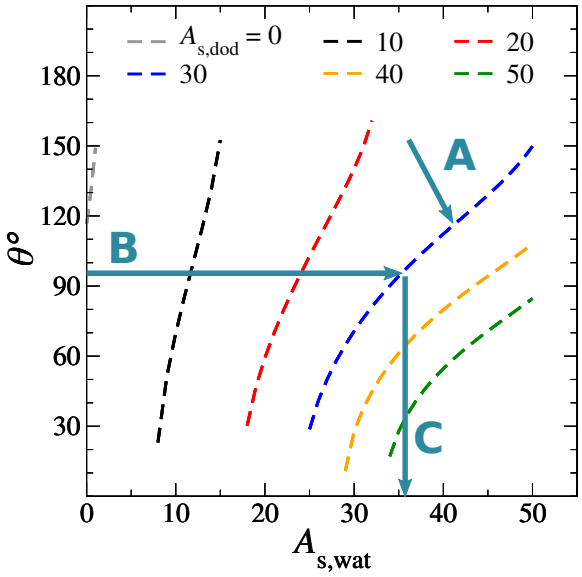

(a) Young contact angles

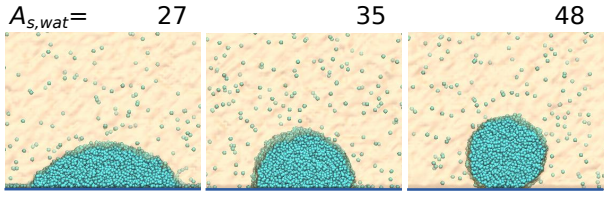

(b) Visualisations

Figure 9: (a) Contact angles from the Young equation for a DPD water droplet in dodecane, the arrows indicate the steps followed in the surface parameterisation. (b) Snapshots of explicit droplet simulations using model surfaces with different hydrophobicity degrees.

Table 5: Details of simulation boxes for the explicit droplet simulations of water droplets in dodecane. For column details see Table 2.

Box ID	$(L_x,\ L_y,\ L_z)$	$(l_x,\ l_y,\ l_z)$	N_{dod}	N_{wat}	N_{tot}
Box1	(78, 26, 32.5)	(13, 26, 13)	28 648	13 183	213 719
Box2	(90, 30, 37.5)	(15, 30, 15)	44 010	20 251	328 321
Box3	(102, 34, 42.5)	(17, 34, 17)	64 065	29 479	477 934
Box4	(114, 38, 47.5)	(19, 38, 19)	89 441	41 155	667 242

Table 6: Experimental contact angles from Andersson *et al.*,[37] and simulated values in this work, for SAMs of different quality. The figure in brackets is an estimate of the error in the final digit.

SAM composition		Exp. θ [°]	$A_{s,\mathrm{wat}}$	Simul. θ [°]
72 % −OH	28 % $-CH_3$	51	27	56 (2)
48 % −OH	52 % $-CH_3$	95	35	97 (2)
22 % −OH	78 % $-CH_3$	139	48	142 (5)

for the cases selected are given in the third column of Table 6.

Finally, we confirm that the surface parametrisation reproduces the target contact angles using explicit droplet simulations. A complete list of the simulated systems is give in Table 5 and the analysis method is applied as described in Sec. 2.4.3. The droplets are shown in Fig. 9b and the measured contact angle values are presented in the last column of Table 6. The results are in good agreement with the experimental values (where the average standard deviation is 6°), with a relative error under 5 %.

4 Conclusions

In this work, we set out to develop the basis for the development of chemically specific surface interactions for dissipative particle dynamics simulation. We compared explicit droplet simulations with independent computations of the contact angle from the Young equation, using separate measurements of the interfacial tension and surface energies, finding good agreement. We then demonstrated how our model can be used to parametrise a SAM-covered silica surface to obtain a given contact angle for a water droplet in dodecane sitting on the

surface. Fig. 9a is the key result here, since it shows how to choose the wall interaction parameters to obtain a specified contact angle in this particular system, but obviously the method can be applied to other systems. Our results show that surfaces can be easily and rapidly parametrised *via* the surface energies, which are computable with a relatively trivial extension of the pressure tensor method for computing the interfacial tension between liquids. Realistic surfaces can be modelled by tuning the interactions between DPD beads and the wall, using experimental contact angles as a benchmark, without having to undertake expensive explicit droplet simulations for calibration. We have focussed on flat, structureless surfaces but in principle the methods can be extended to structured surfaces, although the computation of the surface energies becomes complicated if one has to implement a 'phantom wall' and lift it off the surface, in a thermodynamic integration step.[27–29]

We now outline a number of avenues for future work. To continue in the above direction, we have started to explore how density functional theory (DFT) may be used to compute the surface energies and density profiles within our wall models, which would obviate the need to undertake any simulations at all. One interesting result of this is that with a simple mean-field DFT, one can devise a wall potential for which the water model (as a fluid of DPD water beads at a specified density) is predicted to be completely structureless away from the wall, or in other words have a flat density profile. We further find that the required wall potential can be interpreted as corresponding to a 'DPD continuum' made from DPD water beads at the bulk water bead density, in the $z < 0$ half space. This provides a theoretical justification for the approach of Goicochea and Alarcón, who first developed this concept.[38]

Additionally, not investigated in the present work, one can ask how the individual molecular groups are distributed in the vicinity of the wall. For example, one might expect that for the pure oil, the terminal $-CH_3$ beads in our dodecane model could be preferentially located at the wall, on purely entropic grounds.[39] Microscopically, the local structure can be controlled to some extent by adjusting the individual DPD bead wall interactions. In the present work, for simplicity we did not distinguish between the two hydrocarbon bead types

in this respect, but in future works these could be fine-tuned to reproduce the molecular density profiles in greater detail.

Finally, our studies could be extended to include the kinetics of wetting, spreading, and detachment. The fluids in our DPD models have well-defined viscosities, and so in principle one ought to be able to investigate these dynamical aspects with the current models. In our flat, structureless wall model though, the wall potential gives rise to forces on the DPD beads which are normal to the surface, and thus there are no lateral forces. As it stands therefore, there is nothing to stop the bulk DPD fluid from sliding freely over the wall, which would appear to be completely frictionless. To remove this 'feature', one could introduce lateral wall friction forces along the lines of the interparticle dissipative forces between DPD particles, with a corresponding fluctuating wall force to satisfy the fluctuation-dissipation theorem.[40] With this, one can hope to be able to control and adjust the hydrodynamic slip length at the wall, without perturbing the equilibrium structural features such as the surface energies and the contact angle. The movement of the contact line in such models would additionally need to be characterised, and related to the mesoscopic physics of the real system that the model was attempting to emulate.[41]

Acknowledgements

This work was in part funded by Unilever PLC and the STFC Hartree Centre's *Innovation: Return on Research programme*, funded by the UK Department for Business, Energy & Industrial Strategy.

Appendix: force balance considerations

In this Appendix we establish an operational definition of the surface energy at a wall such that the Young equation for a droplet on a surface is automatically satisfied, then confirm the validity of Eq. (7) in the main text, specifying how the wall forces should be incorporated

into the appropriate component of the pressure tensor.

Consider a cylindrical droplet sitting on the lower surface of a simulation box, between two confining walls, as shown in Fig. 10. Let the droplet have height H and the contact angle be θ, and consider two planes AA$'$ and BB$'$ extending across the simulation box as indicated in Fig. 10a, with the latter intersecting the droplet at its maximum height. The force across AA$'$ will be $p_1 L_z - 2\gamma_{s1}$ and similarly the force across BB$'$ will be $p_2 H + p_1(L_z - H) - \gamma_{s2} - \gamma_{12} - \gamma_{s1}$, where p_1 and p_2 are the pressures outside and inside the droplet, the corresponding surface energies are γ_{s1} and γ_{s2}, and the interfacial tension is γ_{12}. We suppose that the scale is macroscopic, so that the interfaces are infinitely thin on the length scale of the droplet. Assuming force balance we therefore have $p_1 L_z - 2\gamma_{s1} = p_2 H + p_1(L_z - H) - \gamma_{s2} - \gamma_{12} - \gamma_{s1}$. We note that the pressure inside the droplet exceeds the external pressure by an amount given by the Laplace equation, so that $p_2 - p_1 = \gamma_{12}/R$, where R is the radius of the droplet. The above force balance then simplifies to $\gamma_{s1} = \gamma_{s2} + \gamma_{12}(1 - H/R)$. It follows from elementary Euclidean geometry that if the droplet profile is considered as an arc of a circle, the half-angle subtended by the 'footprint' of the droplet on the surface at the centre of this circle is equal to the contact angle as indicated in Fig. 10b.[42] This implies $H = R(1 - \cos\theta)$, and so we recover the Young equation as given in Eq. (1) in the main text.

The implication is that the total force transmitted across a plane like AA$'$ can be used to make an operational definition of the surface energy γ_z such that the Young equation is satisfied, at least macroscopically. The plane should extend far enough above and below the simulation box to encompass all the forces present. For our purposes, since there are no forces outside the hard reflecting boundaries we need only consider the force transmitted across the segment contained between these boundaries.

Now remove the droplet and consider a simulation box containing pure fluid bounded by walls top and bottom, as in the left hand part of Fig. 10a. In this situation we could place the AA$'$ plane anywhere in the simulation box and we should end up with the same transmitted force, so that we can conclude the force transmitted across such a plane can

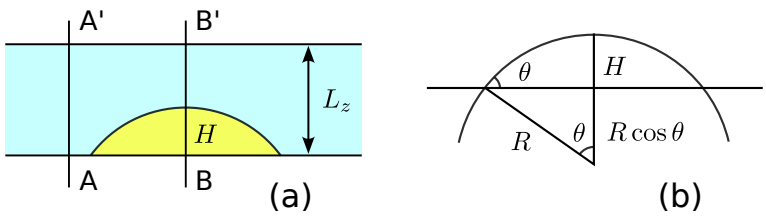

Figure 10: A cylindrical droplet on a surface: (a) the force across AA′ must match the force across BB′; (b) the geometry of the droplet.

be written as $L_z\langle P_{xx}\rangle$, where $\langle P_{xx}\rangle$ is the volume-average component of the pressure tensor in the direction parallel to the surface. This now furnishes us with a precise definition of the surface energy, namely $2\gamma_s = L_z(p - \langle P_{xx}\rangle)$, noting there are two walls at the top and bottom of the control volume (Fig. 10a). Since the fluid is isotropic and $\langle P_{xx}\rangle = \langle P_{yy}\rangle$, one can also write this as $2\gamma_s = L_z(p - (\langle P_{xx}\rangle + \langle P_{yy}\rangle)/2)$.

This definition assumes that we know the bulk pressure but in practice we want to avoid having to measure this separately or rely on the barostat. A careful analysis of the force balance normal to the substrate allows us to do exactly this. The starting point is the macroscopic hydrostatic equation, $\partial P_{zz}/\partial z - f_z^{\text{ext}} = 0$, where f_z^{ext} is the external force density exerted by the walls on the fluid. In microscopic terms, this force density is $f_z^{\text{ext}} = \sum_i F_{i,z}^{\text{ext}}\,\delta(\vec{r} - \vec{r}_i) = (1/A)\sum_i F_{i,z}^{\text{ext}}\,\delta(z - z_i)$, where $F_{i,z}^{\text{ext}}$ is the external force exerted by the wall on the i-th particle, and we exploit the fact that on average f_z^{ext} should be independent of position in the lateral direction to replace it by an area average, with $A = L_xL_y$.

Let us integrate the hydrostatic pressure equation, from some point $z = L$ in the bulk where $P_{zz} \to p$, towards the surface at $z = 0$. We obtain in this way $p = P_{zz}(z) + \int_z^L \mathrm{d}z\, f_z^{\text{ext}}$. Injecting the microscopic expression for the force density into this obtains

$$p = P_{zz}(z) + \frac{1}{A}\sum_i F_{i,z}^{\text{ext}}\,\Theta(z_i - z)\,\Theta(L - z_i)\,, \tag{10}$$

where the Θ-functions ensure that only particles with $z < z_i < L$ are counted. We integrate

once more in the z-direction, using the fact that $\int_0^L \mathrm{d}z\,\Theta(z_i - z) = z_i$ if $z_i < L$, to obtain

$$p = \frac{1}{L}\int_0^L \mathrm{d}z\,P_{zz} + \frac{1}{AL}\sum_i F_{i,z}^{\mathrm{ext}}\,z_i\,\Theta(L - z_i)\,. \tag{11}$$

As mentioned, the height L in here should be large enough to warrant the assumption that one is in the bulk (where, in fact, $F_{i,z}^{\mathrm{ext}} = 0$ anyway), but not so large as to reach the upper confining wall. However, we can make the exact same argument for this upper confining wall, and combining the expressions yields

$$p = \langle P_{zz}\rangle + \frac{1}{V}\sum_{i,\mathrm{lower}} F_{i,z}^{\mathrm{ext}}\,z_i + \frac{1}{V}\sum_{i,\mathrm{upper}} F_{i,z}^{\mathrm{ext}}\,(L_z - z_i)\,, \tag{12}$$

noting that the limited range of the wall force obviates the need to retain Θ-functions. Here $\langle P_{zz}\rangle$ is the volume-average component of the conventionally-defined pressure tensor in the z-direction normal to the surface. Treated as an expression for p, this can now be injected into the above definition of the surface energy to obtain the final result

$$\gamma_s = \frac{L_z}{2}\Big(\langle P'_{zz}\rangle - \frac{1}{2}(\langle P_{xx}\rangle + \langle P_{yy}\rangle)\Big)\,, \tag{13}$$

where, to be explicit,

$$\begin{aligned}
\langle P_{xx}\rangle &= \Big\langle \frac{1}{V}\sum_{i>j} F_{ij,x}(x_j - x_i)\Big\rangle\,, \qquad \langle P_{yy}\rangle = \Big\langle \frac{1}{V}\sum_{i>j} F_{ij,y}(y_j - y_i)\Big\rangle\,,\\
\langle P'_{zz}\rangle &= \Big\langle \frac{1}{V}\sum_{i>j} F_{ij,z}(z_j - z_i)\Big\rangle + \Big\langle \frac{1}{V}\sum_{i,\mathrm{lower}} F_{i,z}^{\mathrm{ext}}\,z_i\Big\rangle + \Big\langle \frac{1}{V}\sum_{i,\mathrm{upper}} F_{i,z}^{\mathrm{ext}}\,(L_z - z_i)\Big\rangle\,.
\end{aligned} \tag{14}$$

In these $\vec{F}_{ij}$ is the force between the i-th and j-th particles so that the first terms are the conventional virial pressure tensor components. Additionally, $\langle\cdots\rangle$ can be taken to be an ensemble average as well as the indicated volume average. Apart from the formal inclusion of the external forces into P'_{zz}, this is identical to Eq. (7) in the main text and justifies its use for the surface energy at the wall.

The theory leading to these final results in Eqs. (13) and (14) rests on the assumptions that there are no particles outside the hard walls, and that the external forces exerted by the walls are only in the z-direction normal to the walls. Without these, such as would be the case where the walls are represented by frozen or tethered particles, the problem would have to be revisited.

Note that the kinetic contributions can be omitted from the pressure tensor components in Eq. (14). This is justified because the kinetic part of the pressure tensor is isotropic even in an inhomogeneous fluid (the momenta of the particles remain decoupled in the Hamiltonian even if the particles are acted on by an external force). This is also the case for the usual expression for the surface tension of a liquid-liquid interface.

References

(1) Anderson, R. L.; Bray, D. J.; Ferrante, A. S.; Noro, M. G.; Stott, I. P.; Warren, P. B. Dissipative particle dynamics: systematic parametrization using water-octanol partition coefficients. *J. Chem. Phys.* **2017**, *147*, 094503.

(2) Anderson, R. L.; Bray, D. J.; Del Regno, A.; Seaton, M. A.; Ferrante, A. S.; Warren, P. B. Micelle formation in alkyl sulfate surfactants using dissipative particle dynamics. *J. Chem. Theory Comput.* **2018**, *14*, 2633–2643.

(3) Del Regno, A.; Warren, P. B.; Bray, D. J.; Anderson, R. L. Critical micelle concentrations in surfactant mixtures and blends by simulation. *J. Phys. Chem. B* **2021**, *125*, 5983–5990.

(4) Anderson, R. L.; Gunn, D. S. D.; Taddese, T.; Lavagnini, E.; Warren, P. B.; Bray, D. J. Phase behavior of alkyl ethoxylate surfactants in a dissipative particle dynamics model. *J. Phys. Chem. B* **2023**, *127*, 1674–1687.

(5) Bray, D. J.; Anderson, R. L.; Warren, P. B.; Lewtas, K. Wax formation in linear and

branched alkanes with dissipative particle dynamics. *J. Chem. Theory Comput.* **2020**, *16*, 7109–7122.

(6) Bray, D. J.; Anderson, R. L.; Warren, P. B.; Lewtas, K. Modeling alkyl aromatic hydrocarbons with dissipative particle dynamics. *J. Phys. Chem. B* **2022**, *126*, 5351–5361.

(7) Suttipong, M.; Grady, B. P.; Striolo, A. Surfactants adsorption on crossing stripes and steps. *Soft Matter* **2017**, *13*, 862–874.

(8) Striolo, A. Studying surfactants adsorption on heterogeneous substrates. *Curr. Opin. Chem. Eng.* **2019**, *23*, 115–122.

(9) Klebes, J.; Finnigan, S.; Bray, D. J.; Anderson, R. L.; Swope, W. C.; Johnston, M. A.; Conchuir, B. O. The role of chemical heterogeneity in surfactant adsorption at solid–liquid interfaces. *J. Chem. Theory Comput.* **2020**, *16*, 7135–7147.

(10) Jiang, H.; Patel, A. J. Recent advances in estimating contact angles using molecular simulations and enhanced sampling methods. *Curr. Opin. Chem. Eng.* **2019**, *23*, 130–137.

(11) Young, T. An essay on the cohesion of fluids. *Phil. Trans. R. Soc.* **1805**, *95*, 65–87.

(12) de Gennes, P.-G. Wetting: statics and dynamics. *Rev. Mod. Phys.* **1985**, *57*, 827–863.

(13) de Gennes, P.-G.; Brochard-Wyart, F.; Quéré, D. *Capillarity and Wetting Phenomena*; Springer: New York, 2003.

(14) Dillan, K. W.; Goddard, E. D.; McKenzie, D. A. Oily soil removal from a polyester substrate by aqueous nonionic surfactant systems. *J. Am. Oil Chem. Soc.* **1979**, *56*, 59–70.

(15) Frye, G. C.; Berg, J. C. Antifoam action by solid particles. *J. Coll. Interf. Sci.* **1989**, *127*, 222–238.

(16) Yang, Y.; Fang, Z.; Chen, X.; Zhang, W.; Xie, Y.; Chen, Y.; Liu, Z.; Yuan, W. An overview of Pickering emulsions: solid-particle materials, classification, morphology, and applications. *Front. Pharmacol.* **2017**, *8*, 287.

(17) Wills, B. A.; Napier-Munn, T. *Wills' Mineral Processing Technology An Introduction to the Practical Aspects of Ore Treatment and Mineral Recovery, 7th Edition*; Elsevier: Amsterdam, 2006.

(18) Groot, R. D.; Warren, P. B. Dissipative particle dynamics: bridging the gap between atomistic and mesoscopic simulation. *J. Chem. Phys.* **1997**, *107*, 4423–4435.

(19) Español, P.; Warren, P. B. Perspective: dissipative particle dynamics. *J. Chem. Phys.* **2017**, *146*, 150901.

(20) Venturoli, M.; Smit, B. Simulating the self-assembly of model membranes. *Phys. Chem. Comm.* **1999**, *2*, 45–49.

(21) Venturoli, M.; Sperotto, M. M.; Kranenburg, M.; Smit, B. Mesoscopic models of biological membranes. *Phys. Rep.* **2006**, *437*, 1–54.

(22) Warren, P. B.; Prinsen, P.; Michels, M. A. J. The physics of surfactant dissolution. *Phil. Trans. R. Soc.* **2003**, *361*, 665–676.

(23) Seaton, M. A.; Anderson, R. L.; Metz, S.; Smith, W. DL_MESO: highly scalable mesoscale simulations. *Mol. Simul.* **2013**, *39*, 796–821.

(24) Abascal, J. L.; Vega, C. A general purpose model for the condensed phases of water: TIP4P/2005. *J. Chem. Phys.* **2005**, *123*, 234505.

(25) Siu, S. W. I.; Pluhackova, K.; Böckmann, R. A. Optimization of the OPLS-AA force field for long hydrocarbons. *J. Chem. Theory Comput.* **2012**, *8*, 1459–1470.

(26) Kirkwood, J. G.; Buff, F. P. The statistical mechanical theory of surface tension. *J. Chem. Phys.* **1949**, *17*, 338–343.

(27) Leroy, F.; dos Santos, D. J. V. A.; Müller-Plathe, F. Interfacial excess free energies of solid–liquid interfaces by molecular dynamics simulation and thermodynamic integration. *Macromol. Rapid Comm.* **2009**, *30*, 864–870.

(28) Leroy, F.; Müller-Plathe, F. Solid-liquid surface free energy of Lennard-Jones liquid on smooth and rough surfaces computed by molecular dynamics using the phantom-wall method. *J. Chem. Phys.* **2010**, *133*, 044110.

(29) Jiang, H.; Müller-Plathe, F.; Panagiotopoulos, A. Z. Contact angles from Young's equation in molecular dynamics simulations. *J. Chem. Phys.* **2017**, *147*, 084708.

(30) Thomas, S. M.; Chan, Y. T. A simple approach for the estimation of circular arc center and its radius. *Comput. Vision Graph.* **1989**, *45*, 362–370.

(31) Zhang, J.; Wang, P.; Borg, M. K.; Reese, J. M.; Wen, D. A critical assessment of the line tension determined by the modified Young's equation. *Phys. Fluids* **2018**, *30*, 082003.

(32) Jańczuk, B.; Wójcik, W.; Zdziennicka, A. Determination of the components of the surface tension of some liquids from interfacial liquid-liquid tension measurements. *J. Coll. Interf. Sci.* **1993**, *157*, 384–393.

(33) Zeppieri, S.; Rodríguez, J.; López de Ramos, A. L. Interfacial tension of alkane + water systems. *J. Chem. Eng. Data* **2001**, *46*, 1086–1088.

(34) Khedr, A.; Striolo, A. DPD parameters estimation for simultaneously simulating water–oil interfaces and aqueous nonionic surfactants. *J. Chem. Theory Comput.* **2018**, *14*, 6460–6471.

(35) Steinmetz, D.; Creton, B.; Lachet, V.; Rousseau, B.; Nieto-Draghi, C. Simulations of interfacial tension of liquid–liquid ternary mixtures using optimized parametrization for coarse-grained models. *J. Chem. Theory Comput.* **2018**, *14*, 4438–4454.

(36) Alasiri, H. S.; Sultan, A. S.; Chapman, W. G. Effect of surfactant headgroup, salts, and temperature on interfacial properties: dissipative particle dynamics and experiment for the water/octane/surfactant system. *Energ. Fuel.* **2019**, *33*, 6678–6688.

(37) Andersson, M.; Hassenkam, T.; Matthiesen, J.; Nikolajsen, L.; Okhrimenko, D. V.; Dobberschutz, S.; Stipp, S. L. First-principles prediction of surface wetting. *Langmuir* **2020**, *36*, 12451–12459.

(38) Goicochea, A. G.; Alarcón, F. Solvation force induced by short range, exact dissipative particle dynamics effective surfaces on a simple fluid and on polymer brushes. *J. Chem. Phys.* **2011**, *134*, 014703.

(39) Fleer, G. J.; Cohen Stuart, M. A.; Scheutjens, J. M. H. M.; Cosgrove, T.; Vincent, B. *Polymers at Interfaces*; Springer: New York, 1993.

(40) Español, P.; Warren, P. Statistical mechanics of dissipative particle dynamics. *Europhys. Lett.* **1995**, *30*, 191–196.

(41) Mohammad Karim, A. A review of physics of moving contact line dynamics models and its applications in interfacial science. *J. Appl. Phys.* **2022**, *132*, 080701.

(42) Heath, T. L. *Euclid's Elements*; Dover: New York, 1956; The relevant geometric propositions are from Book III: if a line be tangent to a circle, and from the point of contact a chord be drawn cutting the circle (here, the 'footprint' of the droplet), the angle made by this chord with the tangent (*i. e.* the contact angle) is equal to the angle subtended by the chord in the alternate segment of the circle (Prop. 32), which is equal to the half-angle subtended at the centre of the circle (Prop. 20).